ACS APPLIED ENERGY MATERIALS

www.acsaem.org Letter

All-Solid-State Batteries Using Rationally Designed Garnet Electrolyte Frameworks

Eongyu Yi, Hao Shen, Stephen Heywood, Judith Alvarado, Dilworth Y. Parkinson, Guoying Chen, Stephen W. Sofie, and Marca M. Doeff*

Cite This: https://dx.doi.org/10.1021/acsaem.9b02101 Read Online

ACCESS | Metrics & More | Article Recommendations | Supporting Information

ABSTRACT: Functioning bulk-type all-solid-state batteries in a practical form factor with composite positive electrodes, using Al-substituted $Li_7La_3Zr_2O_{12}$ (LLZO) as the solid electrolyte, have been demonstrated for the first time. The devices incorporate bilayers composed of dense LLZO membranes and porous LLZO scaffolds infiltrated with $LiNi_{0.6}Mn_{0.2}Co_{0.2}O_2$ and other components as positive electrodes, combined with lithium anodes. The porous scaffolds are prepared using an easily scaled freeze-tape-casting method. The unidirectional pores of the scaffold facilitate infiltration of cathode components and shorten lithium ion diffusion path lengths, while the addition of a soft ionically conductive solid to the scaffold ensures good contact among the components.

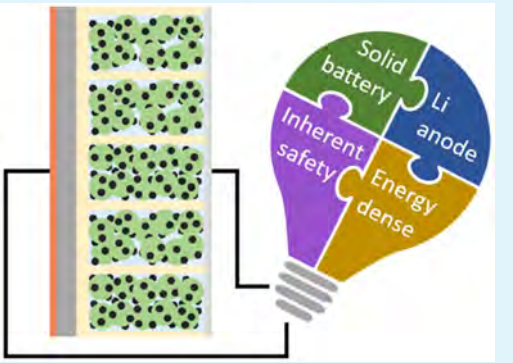

KEYWORDS: *solid-state battery, solid electrolyte, freeze-tape-casting (FTC), tape-casting, LLZO garnet*

All-solid-state batteries (ASSBs) potentially offer higher energy density, longer cycle life, and better inherent safety than state-of-the-art lithium ion batteries (LIBs).[1] However, successful fabrication of ASSBs with ceramic electrolytes has primarily been restricted to small-scale thin film devices due to processing difficulties and interfacial challenges.[2] Here, we address these issues by combining tape-casting and freeze-tape-casting (FTC) methods to construct porous/dense and porous/dense/porous bi/trilayer $Li_7La_3Zr_2O_{12}$ (LLZO) frameworks in which the porous layers are composed of vertically aligned LLZO walls functioning as directional ion conduction pathways. ASSBs are constructed by infiltrating active material and other components into the porous layers and adhering lithium metal to the dense side of the bilayer framework. We also reduced the cathode/LLZO interfacial impedance by introducing a plastic-crystal solid electrolyte into the porous layers. No liquid electrolytes were added to these devices to make them function.

LLZO was selected due to its high ionic conductivity (0.1–1.3 mS cm^{-1}), wide electrochemical stability window (~6 V), chemical stability to Li, and dry air stability.[3] FTC, a combination of freeze-casting and tape-casting, is a scalable method for making thin porous films, with good control over total pore volume, pore size, and morphology.[4] In addition, tape thicknesses ranging from several millimeters to <100 μm can be fabricated, while retaining pore alignment throughout the thickness. A key feature of the FTC prepared LLZO scaffolds is the low tortuosity (approaching unity) pore channels along the thickness direction, which aids infiltration and shortens Li diffusion path lengths.[5] Furthermore, structurally resilient FTC-LLZO scaffolds can be readily prepared at very high porosities in the green state, exceeding 90%, compared to methods using traditional pore-forming fugitives. The FTC process is also environmentally friendly as ice crystals function as the pore-former, not polymers, which generate CO_2 during burnout. Another crucial factor aiding device design is the incorporation of a plastic-crystal solid electrolyte into the pores, which acts as a mediator to connect the cathode material and the LLZO, thus avoiding the need for cosintering and associated deleterious reactions that may occur at high temperature. This also reduces interfacial impedance and permits stable operation of the ASSBs.

Figure 1 shows the process for making freestanding dense LLZO films, used as the separators/electrolytes in symmetrical cell cycling. Powders were first ball-milled to reduce and homogenize the particle size, and excess Li_2CO_3 was added to compensate for lithium loss during the high temperature sintering process. The amount of excess needed is dependent upon the desired sample thickness.[6,7] The phase purity and microstructure of the sintered films are sensitive to temperature (Figure S1). Nearly transparent, phase-pure, and pinhole-free LLZO films with approximately 95% density and 25–44

Received: October 25, 2019
Accepted: January 2, 2020
Published: January 2, 2020

https://dx.doi.org/10.1021/acsaem.9b02101
ACS Appl. Energy Mater. XXXX, XXX, XXX–XXX

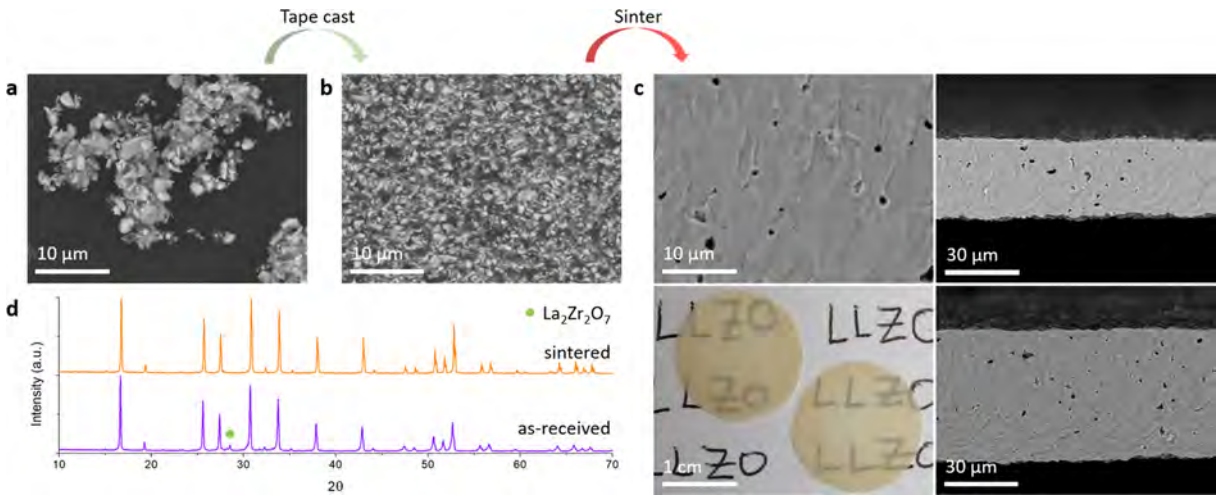

Figure 1. (a) SEM image of as-received LLZO powder. (b) SEM fracture surface image of tape-cast green tape. (c) SEM fracture surface images and optical image of LLZO films sintered in optimal sintering profile. (d) XRD patterns of the as-received powder and the sintered film.

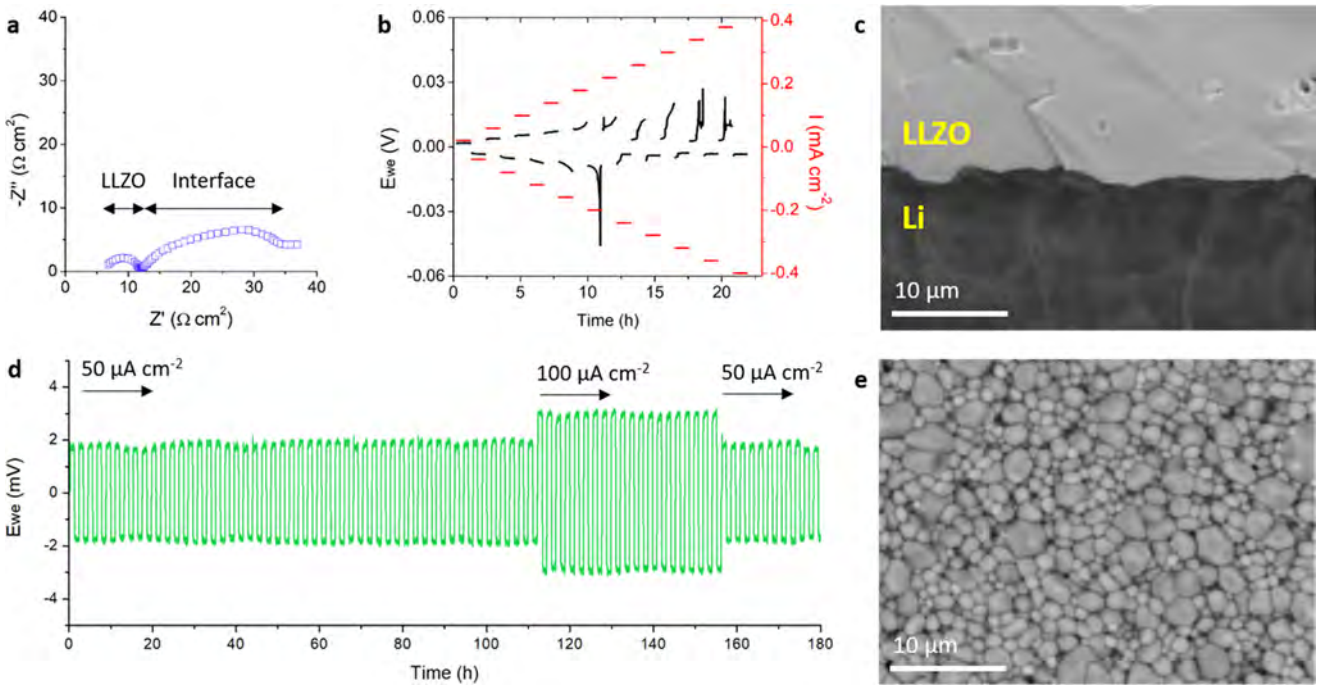

Figure 2. (a) Nyquist plot of Au interface engineered Li/LLZO/Li cell. (b) DC cycling of Au interface engineered Li/LLZO/Li cell with a step current of 20 μA cm^{-2} starting from 20 μA cm^{-2}. (c) SEM fracture surface image showing superior interfacial bonding of Li and LLZO. (d) DC cycling of Au interface engineered Li/LLZO/Li cell at selected current densities. (e) SEM surface image of typical sintered LLZO thin films.

μm thickness could be fabricated successfully once the process was optimized.

Figure 2 shows the electrochemical properties of Li/LLZO/Li cells and microstructural features. Gold was sputter coated on both sides of the LLZO films to reduce the interfacial resistance. Li metal was melt bonded to the Au coated LLZO resulting in intimate contact (Figure 2c). The molten Li wets and spreads on Au as the Li−Au alloying reaction has a large negative Gibbs free energy release.[8]

In Figure 2a, three resistive components are observed in the Nyquist plot of the Li/LLZO/Li cell. The high frequency semicircle corresponds to the LLZO resistance, giving a conductivity of 0.5 mS cm^{-1}. The depressed semicircle at the lower frequency range is a combination of Li−Au alloying and Li−Au/LLZO interfacial impedances.[9] The total cell impedance is only 35 Ω cm^2, with an interfacial impedance of 12 Ω cm^2, comparable to other reported literature values of interface engineered LLZO.[10,11]

Figure 2b shows direct current (DC) cycling of the modified LLZO membrane, stepping the current in increments of 20 μA cm^{-2} starting from 20 μA cm^{-2}. Voltage instability is observed at a critical current density of 0.2 mA cm^{-2}. Cells could be cycled stably at current densities of 50 and 100 μA cm^{-2} (Figure 2d). It is well-known that the voltage instabilities are due to Li dendrite/filament propagation in grain boundaries or within the bulk of LLZO. The current density at which this occurs heavily depends on the processing history and surface treatment/microstructure of sintered LLZO.[12,13]

In contrast, symmetrical cells of untreated LLZO exhibited extremely high cell impedance (>50 kΩ cm^2) along with

https://dx.doi.org/10.1021/acsaem.9b02101
ACS Appl. Energy Mater. XXXX, XXX, XXX−XXX

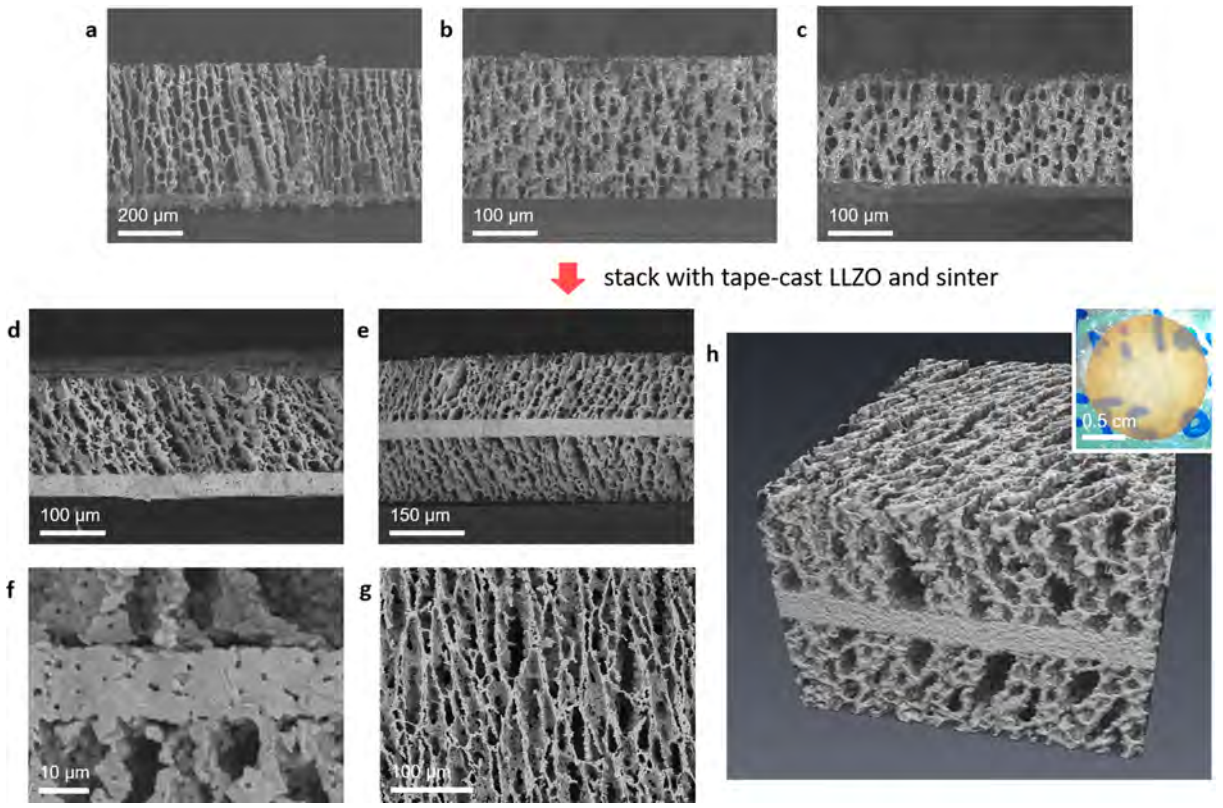

Figure 3. Fracture surface SEM micrographs of green tapes freeze-tape-cast from slurries containing (a) 7.5 vol % LLZO/400 μm, (b) 10 vol % LLZO/220 μm, and (c) 10 vol % LLZO/150 μm. Fracture surface micrographs of (d) sintered porous/dense (140/36 μm) bilayer, (e) porous/dense/porous (130/37/130 μm) trilayer, and (f) porous/dense/porous trilayer with a 14 μm dense layer. (g) Surface SEM micrograph of the porous layer. (h) 3D reconstruction of micro-CT scan of the trilayer. Subvolume size is 400 (width) × 280 (height) × 530 (depth) μm^3. Inset shows an optical image of a typical trilayer.

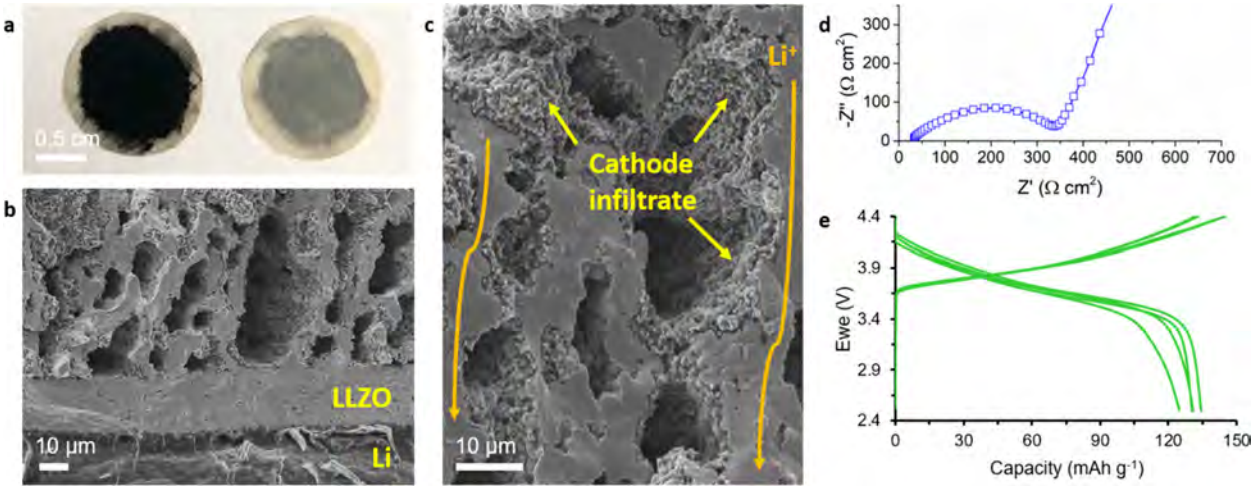

Figure 4. (a) Optical image of cathode-infiltrated LLZO bilayer. Cathode-infiltrated porous layer surface (left) and dense layer surface (right) are shown. (b) SEM fracture surface image of cathode-infiltrated bilayer. Images were taken prior to SCN electrolyte infiltration. (c) Same cell at higher magnification showing cathode-infiltrate. (d) Nyquist plot of the constructed ASSB. (e) Initial charge/discharge voltage profiles of the ASSB.

instantaneous shorting upon DC cycling at 50 μA cm^{-2} (Figure S2). This is fairly typical of cells containing untreated LLZO samples unless pressure is applied (which could not be done here due to the fragility of the thin ceramic samples).[14,15]

Figure 3a–c shows typical cross-sectional fracture surface images of LLZO samples freeze-tape-cast using different conditions. The green tape cast from the 7.5 vol % LLZO slurry (Figure 3a) shows wider spacing between LLZO columns compared to the one cast from 10 vol % LLZO (Figure 3b,c). The lower ceramic loading leads to improved LLZO dispersion and results in fewer ice nucleation sites per unit area, favoring more aligned growth of the ice crystals. Interactions with water at higher loadings foster local agglomeration, which can prevent formation of the desired structures. By adjusting the doctor blade gap, green tapes ranging in thickness from 150 to 400 μm were obtained.

https://dx.doi.org/10.1021/acsaem.9b02101
ACS Appl. Energy Mater. XXXX, XXX, XXX−XXX

FTC and tape-cast green tapes were stacked together and sintered to form porous/dense bilayer and porous/dense/porous trilayer LLZO architectures (Figures 3d–h). Sintering profiles were optimized to achieve phase purity (cubic-LLZO) and high densities. Typical dense layer thicknesses were 25–35 μm and could be reduced down to 14 μm because the thick porous LLZO layers serve as mechanical supports for the otherwise fragile thin dense films. FTC green tapes made with 10 vol % LLZO slurry were used which resulted in 70% porosity once sintered. Trilayers are particularly advantageous here because the symmetry allows for uniform shrinkage during densification. An optical image of a typical trilayer and a 3D reconstruction of a microcomputed tomography (CT) scan are shown in Figure 3h and the Supporting Information video. From these, the unidirectional nature of the pores and the absence of closed pores are evident. Fracture surface images show what might appear to be pore blockages but are due to LLZO rods extending from one wall to another. As can be seen in the top surface image (Figure 3g), the pores are not blocked. Electrode components can be readily infiltrated through the pore openings on the surfaces of the porous layer (Figure 3g). Critical current densities as high as 10 mA cm^{-2} (based on geometric area) have recently been demonstrated in symmetrical cells based on LLZO trilayer structures in which lithium is infiltrated into porous layers with a random pore structure on each side.[16] Increasing the electrode/electrolyte contact area enhances the effective current density greatly compared to devices with planar interfaces.

For this work, ASSBs were constructed using a porous/dense bilayer framework. A slurry containing processed (ball-milled and heat-treated) NMC-622, carbon black, and PVdF binder was infiltrated into the porous layer, followed by solvent removal (Figure 4a). Typical NMC-622 loadings were 4–5 mg cm^{-2} with the potential to reach 35–40 mg cm^{-2} (80–90% of pore occupancy) on further optimization of the infiltration process. Note that these values are for the porous layer used in this study (130 μm thick, 70% porous) and can change with varying porosities and thicknesses of the porous layer. Fracture surface micrographs show that the cathode slurry penetrated into the porous LLZO layer (Figure 4b,c). LiTFSI (4 mol %)/LiBOB (1 mol %)/succinonitrile (SCN) was then melt-infiltrated into the structure. The plastic-crystal electrolyte solidifies on cooling to room temperature and serves as an ionically conducting bridge between the NMC-622 and the LLZO framework as shown in Figure S3. The waxy and soft nature of the plastic-crystal also helps to maintain contact among the components as the cell is cycled.[17,18] In a similar manner, polymer–Li salt complexes (PEO-based) have been reported to electrochemically connect the cathode with sintered oxide solid electrolytes but with limitations on cathode selection (e.g., $LiFePO_4$) and operating temperature ($\geq$60 °C) because of the poor oxidative stability and conductivity of the PEO.[19,20]

The constructed devices showed total room temperature impedances of ~350 Ω cm^2 (Figure 4d), the lowest ever reported for liquid-free ASSBs in practical form factors using LLZO as the electrolyte. Considering that the impedances of the dense LLZO layer and Li/LLZO interfaces are low (Figure 2a), the main contributor is the composite cathode, which is about 120–130 μm thick. Bilayer cells with no SCN-based solid electrolyte infiltration showed total impedances of ~180 kΩ cm^2, demonstrating the crucial role of the mediator solid electrolyte.

The solid-state cells were cycled between 2.5 and 4.4 V at 0.1C (1C = 175 mAh g^{-1}) rate (Figure 4e) and showed discharge capacities of 125–135 mAh g^{-1}. This is comparable to the capacity that is obtained upon cycling processed NMC-622 with liquid electrolyte (Figure S4). Although the structure of the bulk NMC-622 appears unchanged after ball-milling and heat-treatment, some degradation, particularly at particle surfaces, is known to occur, which accounts for the somewhat lower than expected capacity.[21]

Rapid capacity fade within several cycles or much lower than expected capacities are typically reported for ASSBs in which the cathode material and oxide solid electrolyte are heat-treated to ensure intimate contact.[22–25] Absence of conductive additive, formation of electrochemically inactive interfaces, and microcracking due to volume changes during cycling are the likely causes.[22,24] Our preliminary cycling results are in striking contrast, in spite of the use of a thick cathode, 4–6 times thicker than usual.

To the best of our knowledge, this is the first report of successful room temperature cycling of a bulk-type ASSB using a LLZO separator and composite electrode in a practical form factor.[26] Reference 26 contains a comprehensive table listing reports of batteries utilizing garnet electrolytes as of the current year. Almost all studies reporting solid-state batteries use thick LLZO pellets (3–5 mm) and apply/attach active materials to complete a cell. While those studies are useful for answering fundamental questions, they are not in a practical form factor. The use of thick pellets and thin cathode layers greatly compromises energy density. The LLZO should be in a thin film form, the thinner the better, to minimize weight and volume as well as impedance. Examples of LLZO thin films or bilayer/trilayer architectures involving a thin LLZO layer have been reported previously. However, the constructed cells all use liquid electrolytes to address the cathode/LLZO interfacial contact issue and hence should be considered as hybrid cells, not true solid-state cells.[16,27–29]

The superior electrochemical performance of the ASSB constructed here can be ascribed to several factors, including the use of a thin, dense LLZO separator layer, a seamless Li/LLZO contact, a low tortuosity pore structure, and intimate NMC-622/SCN/LLZO contact. In addition to the aforementioned advantages of this approach, the concept of combining a rigid scaffold with a soft, yet solid, conductor is quite general, and can be expanded to other types of solid electrolytes, including those that conduct, e.g., sodium.

Our calculations (Supporting Information and Figure S5) show that ASSBs based on this concept can exceed the energy densities and specific energies of state-of-the-art LIBs by 1.8–2.6 times and 1.2–1.8 times, respectively, if thick electrodes with high porosities are used, the dense LLZO layer is 20 μm thick, and the lithium metal excess is limited to 20%.[30] Our future work will focus on optimizing components to maximize energy density and specific energy, including further tuning of the FTC process.

■ ASSOCIATED CONTENT

Supporting Information

The Supporting Information is available free of charge at https://pubs.acs.org/doi/10.1021/acsaem.9b02101.

Experimental methods and additional figures/data (PDF)

Tomography video (AVI)

https://dx.doi.org/10.1021/acsaem.9b02101
ACS Appl. Energy Mater. XXXX, XXX, XXX–XXX

Gravimetric/volumetric energy density calculator (XLSX)

AUTHOR INFORMATION

Corresponding Author

Marca M. Doeff − *Lawrence Berkeley National Laboratory, Berkeley, California;* orcid.org/0000-0002-2148-8047; Email: mmdoeff@lbl.gov

Other Authors

Eongyu Yi − *Lawrence Berkeley National Laboratory, Berkeley, California;* orcid.org/0000-0002-6079-9382

Hao Shen − *Lawrence Berkeley National Laboratory, Berkeley, California, and Xi'an Jiaotong University, Xi'an, China;* orcid.org/0000-0002-1464-2608

Stephen Heywood − *Montana State University, Bozeman, Montana*

Judith Alvarado − *Lawrence Berkeley National Laboratory, Berkeley, California*

Dilworth Y. Parkinson − *Lawrence Berkeley National Laboratory, Berkeley, California;* orcid.org/0000-0002-1817-0716

Guoying Chen − *Lawrence Berkeley National Laboratory, Berkeley, California;* orcid.org/0000-0002-3218-2609

Stephen W. Sofie − *Montana State University, Bozeman, Montana*

Complete contact information is available at: https://pubs.acs.org/10.1021/acsaem.9b02101

Notes

The authors declare no competing financial interest.

ACKNOWLEDGMENTS

This work was supported by the Assistant Secretary for Energy Efficiency and Renewable Energy, Office of Vehicle Technologies of the U.S. Department of Energy, under Contract DE-AC02-05CH11231. This research used resources of the Advanced Light Source, which is a DOE Office of Science User Facility under Contract DE-AC02-05CH11231. This document was prepared as an account of work sponsored by the United States Government. While this document is believed to contain correct information, neither the United States Government nor any agency thereof, nor the Regents of the University of California, nor any of their employees, makes any warranty, express or implied, or assumes any legal responsibility for the accuracy, completeness, or usefulness of any information, apparatus, product, or process disclosed, or represents that its use would not infringe privately owned rights. Reference herein to any specific commercial product, process, or service by its trade name, trademark, manufacturer, or otherwise, does not necessarily constitute or imply its endorsement, recommendation, or favoring by the United States Government or any agency thereof, or the Regents of the University of California. The views and opinions of authors expressed herein do not necessarily state or reflect those of the United States Government or any agency thereof or the Regents of the University of California.

REFERENCES

(1) Shen, H.; Yi, E.; Cheng, L.; Amores, M.; Chen, G.; Sofie, S. W.; Doeff, M. M. Solid-State Electrolyte Considerations for Electric Vehicle Batteries. *Sustain. Energy Fuels* **2019**, *3*, 1647−1659.

(2) Kerman, K.; Luntz, A.; Viswanathan, V.; Chiang, Y. M.; Chen, Z. Review — Practical Challenges Hindering the Development of Solid State Li Ion Batteries. *J. Electrochem. Soc.* **2017**, *164*, A1731−A1744.

(3) Thangadurai, V.; Narayanan, S.; Pinzaru, D. Garnet-Type Solid-State Fast Li Ion Conductors for Li Batteries: Critical Review. *Chem. Soc. Rev.* **2014**, *43*, 4714−4727.

(4) Sofie, S. W. Fabrication of Functionally Graded and Aligned Porosity in Thin Ceramic Substrates with the Novel Freeze-Tape-Casting Process. *J. Am. Ceram. Soc.* **2007**, *90*, 2024−2031.

(5) Shen, H.; Yi, E.; Amores, M.; Cheng, L.; Tamura, N.; Parkinson, D. Y.; Chen, G.; Chen, K.; Doeff, M. Oriented Porous LLZO 3D Structures Obtained by Freeze Casting for Battery Applications. *J. Mater. Chem. A* **2019**, *7*, 20861−20870.

(6) Yi, E.; Wang, W.; Kieffer, J.; Laine, R. M. Flame Made Nanoparticles Permit Processing of Dense, Flexible, Li^+ Conducting Ceramic Electrolyte Thin Films of Cubic-$Li_7La_3Zr_2O_{12}$ (c-LLZO). *J. Mater. Chem. A* **2016**, *4*, 12947−12954.

(7) Yi, E.; Wang, W.; Kieffer, J.; Laine, R. M. Key Parameters Governing the Densification of Cubic-$Li_7La_3Zr_2O_{12}$ Li^+ Conductors. *J. Power Sources* **2017**, *352*, 156−164.

(8) Wang, J.; Wang, H.; Xie, J.; Yang, A.; Pei, A.; Wu, C. L.; Shi, F.; Liu, Y.; Lin, D.; Gong, Y.; Cui, Y. Fundamental Study on the Wetting Property of Liquid Lithium. *Energy Storage Mater.* **2018**, *14*, 345−350.

(9) Tsai, C. L.; Roddatis, V.; Chandran, C. V.; Ma, Q.; Uhlenbruck, S.; Bram, M.; Heitjans, P.; Guillon, O. $Li_7La_3Zr_2O_{12}$ Interface Modification for Li Dendrite Prevention. *ACS Appl. Mater. Interfaces* **2016**, *8*, 10617−10626.

(10) Wang, C.; Gong, Y.; Liu, B.; Fu, K.; Yao, Y.; Hitz, E.; Li, Y.; Dai, J.; Xu, S.; Luo, W.; Wachsman, E. D.; Hu, L. Conformal, Nanoscale ZnO Surface Modification of Garnet-Based Solid-State Electrolyte for Lithium Metal Anodes. *Nano Lett.* **2017**, *17*, 565−571.

(11) Alexander, G. V.; Patra, S.; Sobhan Raj, S. V.; Sugumar, M. K.; Ud Din, M. M.; Murugan, R. Electrodes-Electrolyte Interfacial Engineering for Realizing Room Temperature Lithium Metal Battery Based on Garnet Structured Solid Fast Li^+ Conductors. *J. Power Sources* **2018**, *396*, 764−773.

(12) Manalastas, W.; Rikarte, J.; Chater, R. J.; Brugge, R.; Aguadero, A.; Buannic, L.; Llordés, A.; Aguesse, F.; Kilner, J. Mechanical Failure of Garnet Electrolytes during Li Electrodeposition Observed by In-Operando Microscopy. *J. Power Sources* **2019**, *412*, 287−293.

(13) Porz, L.; Swamy, T.; Sheldon, B. W.; Rettenwander, D.; Frömling, T.; Thaman, H. L.; Berendts, S.; Uecker, R.; Carter, W. C.; Chiang, Y. M. Mechanism of Lithium Metal Penetration through Inorganic Solid Electrolytes. *Adv. Energy Mater.* **2017**, *7*, 1701003.

(14) Sharafi, A.; Meyer, H. M.; Nanda, J.; Wolfenstine, J.; Sakamoto, J. Characterizing the Li-$Li_7La_3Zr_2O_{12}$ Interface Stability and Kinetics as a Function of Temperature and Current Density. *J. Power Sources* **2016**, *302*, 135−139.

(15) Cheng, L.; Crumlin, E. J.; Chen, W.; Qiao, R.; Hou, H.; Franz Lux, S.; Zorba, V.; Russo, R.; Kostecki, R.; Liu, Z.; Persson, K.; Yang, W.; Cabana, J.; Richardson, T.; Chen, G.; Doeff, M. The Origin of High Electrolyte-Electrode Interfacial Resistances in Lithium Cells Containing Garnet Type Solid Electrolytes. *Phys. Chem. Chem. Phys.* **2014**, *16*, 18294−18300.

(16) Hitz, G. T.; McOwen, D. W.; Zhang, L.; Ma, Z.; Fu, Z.; Wen, Y.; Gong, Y.; Dai, J.; Hamann, T. R.; Hu, L.; Wachsman, E. D. High-Rate Lithium Cycling in a Scalable Trilayer Li-Garnet-Electrolyte Architecture. *Mater. Today* **2019**, *22*, 50−57.

(17) Abouimrane, A.; Davidson, I. J. Solid Electrolyte Based on Succinonitrile and LiBOB: Interface Stability and Application in Lithium Batteries. *J. Electrochem. Soc.* **2007**, *154*, A1031−A1034.

(18) Alarco, P.; Abu-lebdeh, Y.; Abouimrane, A.; Armand, M. The Plastic-Crystalline Phase of Succinonitrile as a Universal Matrix for Solid-State Ionic Conductors. *Nat. Mater.* **2004**, *3*, 476−481.

(19) Wu, J. F.; Pang, W. K.; Peterson, V. K.; Wei, L.; Guo, X. Garnet-Type Fast Li-Ion Conductors with High Ionic Conductivities for All-Solid-State Batteries. *ACS Appl. Mater. Interfaces* **2017**, *9*, 12461−12468.
(20) Jiang, Z.; Xie, H.; Wang, S.; Song, X.; Yao, X.; Wang, H. Perovskite Membranes with Vertically Aligned Microchannels for All-Solid-State Lithium Batteries. *Adv. Energy Mater.* **2018**, *8*, 1801433.
(21) Pan, T.; Alvarado, J.; Zhu, J.; Yue, Y.; Xin, H. L.; Nordlund, D.; Lin, F.; Doeff, M. M. Structural Degradation of Layered Cathode Materials in Lithium-Ion Batteries Induced by Ball Milling. *J. Electrochem. Soc.* **2019**, *166*, A1964−A1971.
(22) Wang, D.; Sun, Q.; Luo, J.; Liang, J.; Sun, Y.; Li, R.; Adair, K.; Zhang, L.; Yang, R.; Lu, S.; Huang, H.; Sun, X. Mitigating the Interfacial Degradation in Cathodes for High-Performance Oxide-Based Solid-State Lithium Batteries. *ACS Appl. Mater. Interfaces* **2019**, *11*, 4954−4961.
(23) Park, K.; Yu, B. C.; Jung, J. W.; Li, Y.; Zhou, W.; Gao, H.; Son, S.; Goodenough, J. B. Electrochemical Nature of the Cathode Interface for a Solid-State Lithium-Ion Battery: Interface between $LiCoO_2$ and Garnet-$Li_7La_3Zr_2O_{12}$. *Chem. Mater.* **2016**, *28*, 8051−8059.
(24) Liu, T.; Zhang, Y.; Zhang, X.; Wang, L.; Zhao, S. X.; Lin, Y. H.; Shen, Y.; Luo, J.; Li, L.; Nan, C. W. Enhanced Electrochemical Performance of Bulk Type Oxide Ceramic Lithium Batteries Enabled by Interface Modification. *J. Mater. Chem. A* **2018**, *6*, 4649−4657.
(25) Han, F.; Yue, J.; Chen, C.; Zhao, N.; Fan, X.; Ma, Z.; Gao, T.; Wang, F.; Guo, X.; Wang, C. Interphase Engineering Enabled All-Ceramic Lithium Battery. *Joule* **2018**, *2*, 497−508.
(26) Samson, A. J.; Hofstetter, K.; Bag, S.; Thangadurai, V. A Bird's-Eye View of Li-Stuffed Garnet-Type $Li_7La_3Zr_2O_{12}$ Ceramic Electrolytes for Advanced All-Solid-State Li Batteries. *Energy Environ. Sci.* **2019**, *12*, 2957−2975.
(27) Xu, S.; McOwen, D. W.; Zhang, L.; Hitz, G. T.; Wang, C.; Ma, Z.; Chen, C.; Luo, W.; Dai, J.; Kuang, Y.; Hitz, E. M.; Fu, K.; Gong, Y.; Wachsman, E. D.; Hu, L. All-in-One Lithium-Sulfur Battery Enabled by a Porous-Dense-Porous Garnet Architecture. *Energy Storage Mater.* **2018**, *15*, 458−464.
(28) Liu, B.; Zhang, L.; Xu, S.; McOwen, D. W.; Gong, Y.; Yang, C.; Pastel, G. R.; Xie, H.; Fu, K.; Dai, J.; Chen, C.; Wachsman, E. D.; Hu, L. 3D Lithium Metal Anodes Hosted in Asymmetric Garnet Frameworks toward High Energy Density Batteries. *Energy Storage Mater.* **2018**, *14*, 376−382.
(29) Gong, Y.; Fu, K.; Xu, S.; Dai, J.; Hamann, T. R.; Zhang, L.; Hitz, G. T.; Fu, Z.; Ma, Z.; McOwen, D. W.; Han, X.; Hu, L.; Wachsman, E. D. Lithium-Ion Conductive Ceramic Textile: A New Architecture for Flexible Solid-State Lithium Metal Batteries. *Mater. Today* **2018**, *21*, 594−601.
(30) Albertus, P.; Babinec, S.; Litzelman, S.; Newman, A. Status and Challenges in Enabling the Lithium Metal Electrode for High-Energy and Low-Cost Rechargeable Batteries. *Nat. Energy* **2018**, *3*, 16−21.

https://dx.doi.org/10.1021/acsaem.9b02101
ACS Appl. Energy Mater. XXXX, XXX, XXX−XXX